Strong particle dynamics counteract the nutrient-pumping effect leading to weak carbon flux in a cyclonic eddy

Xiao-Yuan Zhu, Zixiang Yang, Yuyuan Xie [1], Kuanbo Zhou [*], Wei-Lei Wang [*]

State Key Laboratory of Marine Environmental Science & College of Ocean and Earth Sciences, Xiamen University, Xiamen 361102, China

ARTICLE INFO

ABSTRACT

Sinking particles play a crucial role in transferring carbon from the atmosphere to the deep ocean. However, due to intensive particle transformations such as aggregation, disaggregation, and remineralization, only a small portion of the organic carbon produced in the euphotic zone ends up being sequestered in the deep ocean or sediment. Mesoscale eddies can significantly impact the surface ocean nutrient budget, primary production, and carbon export. Despite this, there is still a lack of research on how particle dynamics in eddy-impacted regions affect the efficiency of carbon export. In this study, we used observations of thorium isotopes (^{234}Th and ^{228}Th) and particulate organic carbon (POC) at two stations in the South China Sea (TS1: a decaying-eddy-impacted station and SEATS: an oligotrophic station) and an inverse model to investigate the impact of particle dynamics on particle export efficiency. Our findings indicate that particle remineralization/fragmentation was enhanced inside the eddy, which counteracted the nutrient pumping effect that promotes surface ocean productivity and eventually led to even lower carbon flux compared to the oligotrophic station.

1. Introduction

The ocean plays a vital role in regulating global climate as it has absorbed ~1/3 of the anthropogenic carbon dioxide (CO_2) released since the industrial revolution began (Ciais et al., 2014; Le Quéré et al., 2018), owing partially to the biological carbon pump that converts carbon dioxide to particulate organic carbon (POC) in the euphotic zone and transports part of it to the deep ocean. Annually, the biological carbon pump transports 5–12 Pg C out of the euphotic zone (Boyd and Trull, 2007; Henson et al., 2011; Siegel et al., 2014; Siegel et al., 2023), and about 15–30% of this exported POC is sequestered for hundreds to thousands of years (Guidi et al., 2015; Henson et al., 2012; Martin et al., 1987). Sinking speed and remineralization rates jointly determine the residence time of sinking POC in the water column. Faster sinking speeds can facilitate a quick transport of POC to the deep ocean and sediment, where remineralization is slower. In contrast, more rapid remineralization can convert organic carbon to dissolved inorganic carbon in the surface waters before it sinks into the deep ocean.

Particle fragmentation, whether physical or biological, reduces the efficiency of particle sequestration by decreasing their sinking speed, while also potentially increasing remineralization. Briggs et al. (2020)

demonstrated that fragmentation accounts for about half of the observed loss in large particle flux in the mesopelagic zone (250–950 m). Therefore, it is one of the major processes controlling the fate of sinking POC out of the euphotic zone. However, technically, it is hard to determine in-situ rates of particle fragmentation using direct observations. Geochemical tracers, especially thorium isotopes, are ideal for constraining these rates because 1) they have well-known sources (^{234}Th from ^{238}U and ^{228}Th from ^{228}Ra, with decay rates independent of temperature); 2) they have strong particle affinity making them easily adsorbed onto particles; 3) the isotopes have different half-lives (e.g., $t_{1/2} = 24.1$ days for ^{234}Th and 1.91 years for ^{228}Th) but the same chemical behavior. Using them jointly enables a model to have more degrees of freedom than using a single tracer.

Mesoscale eddies are ubiquitous in the ocean and are one of the vital processes affecting the surface ocean carbon budget. In the oligotrophic Sargasso Sea, nutrient intrusion from eddy pumping can support up to 50% of new production (McGillicuddy et al., 1998). Such eddy-induced nutrient intrusion may stimulate the growth of phytoplankton, enhance primary production, change the community structure, and ultimately alter particle export fluxes (Benitez-Nelson et al., 2007; Falkowski et al., 1991; Zhou et al., 2020). The cascade response of the marine ecosystem

---
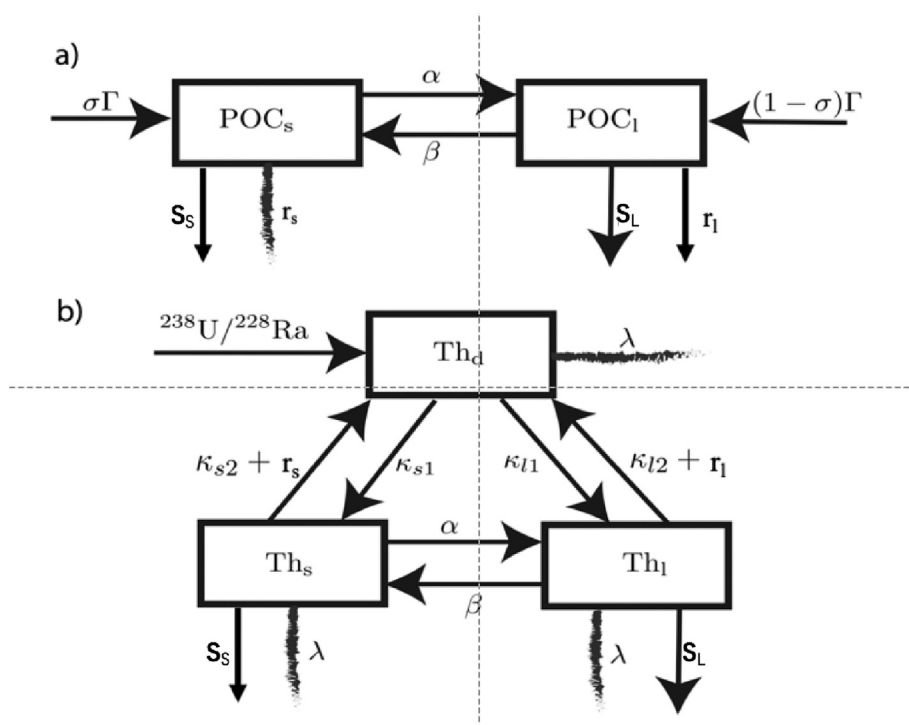
Fig. 1. Conceptual models for the cycling of POC and thorium. σ is the parameter that determines the allocation of production (Γ) to small- or large-sized particles; λ is decay constants for ^{234}Th or ^{228}Th; α and β are aggregation and disaggregation rate constants, respectively; $\mathbf{S}$ is particle divergence operator, which is built based on an exponential decay function; γ is thorium dissolution rate constant. κ_{l1} and κ_{s1} are adsorption rate constants for large and small particles, respectively; κ_{l2} and κ_{s2} are desorption rate constants for large and small particles, respectively; The optimal parameter values and corresponding error bars ($\pm 1\sigma$) are displayed in Table 2.

to eddies will surely change the particle dynamics (including aggregation/disaggregation, remineralization/dissolution, and sinking speed) within eddy-impacted regions. However, studies have yet to be carried out to examine particle dynamics under the influence of mesoscale eddies.

Moreover, Zhou et al. (2020) discovered that the POC flux in a decaying cyclonic eddy was lower in comparison to more oligotrophic stations, potentially due to a higher bacterial respiration rate. To gain a deeper understanding of particle dynamics and related key processes, as well as the role played by eddies in ocean biogeochemistry, we constructed a 1D inverse model that integrates the cycling of POC and two thorium isotopes (^{234}Th and ^{228}Th) from two data sets. One data set was obtained from the center of a decaying cyclonic eddy, and the other was obtained from a nearby oligotrophic station. The goal of the study is to reveal the processes controlling POC flux by constraining the crucial parameters that regulate particle cycling.

2. Materials and methods

2.1. Sample collections

Samples in this study were collected onboard the R/V Dongfanghong II in August 2007 at Station TS1 (111.76°E, 14.28°N) in the center of a cyclonic eddy C1 at its decaying stage (see details in Zhou et al. (2020)), and at Station SEATS (The South East Asian Time-series Study; 116°E, 18°N) located in a non-eddy region of the northern South China Sea (Supplementary Fig. S1). For both stations, 500–1000 L seawater was filtered at discrete depths in the upper 1000 m using in-situ pumps (McLane Research Labs, Falmouth, MA). Seawater was pumped sequentially through a 53 μm Nitex screen (142 mm diameter), a 10 μm Nitex screen (142 mm diameter), and then a 1.0 μm (nominal pore size) quartz fiber filter (QMA, Whatman) to collect size-fractionated particles. Two 12.7 cm MnO$_2$-impregnated cartridges connected in series were used in the pump to scavenge dissolved Th and Ra isotopes. Pump flow rates were 4–7 L min^{-1}. At the same time, 4 L of seawater was collected for total ^{234}Th analyses from the same depths using Niskin bottles attached to a CTD rosette sampler. Samples were collected at eight

depths ranging from 10 to 500 m at station SEATS, and at twelve depths ranging from 10 to 1500 m at TS1. To ensure consistency, we use data from 10 to 500 m at both sites in our inverse model.

2.2. ^{234}Th, ^{228}Th, ^{228}Ra, and ^{238}U analyses

Analysis of total ^{234}Th in the 4-L Niskin samples was based on the small-volume MnO$_2$ co-precipitation technique (Zhou et al., 2020). Size-fractionated pump particles collected on the 53 and 10 μm Nitex screens and on the 1.0 μm QMA filter were processed and analyzed for ^{234}Th as in Cai et al. (2006). Dissolved ^{228}Th and size-fractionated particulate ^{228}Th were determined according to Cai et al.'s protocol (Cai et al., 2006).

^{228}Ra activities in the MnO$_2$ cartridges were measured by analyzing the ^{228}Th daughter approximately 1 yr after the separation of ^{228}Ra from ^{228}Th (e.g., Luo et al., 1995). The collection efficiency of dissolved ^{228}Th on the MnO$_2$ cartridges was estimated from the comparison of ^{234}Th measurements on the MnO$_2$ cartridges and in the small-volume seawater (Cai et al., 2006). Radium collection efficiency on the MnO$_2$ cartridge pair was assumed to be 100% unity. However, the collection efficiency on a single MnO$_2$ cartridge has been demonstrated to be lower than 100% in the GEOTRACES radium inter-calibration program (Charette et al., 2012). Under this assumption, the final ^{228}Ra activities were calculated as the sum of ^{228}Ra measurements on the first and second MnO$_2$ cartridges. To verify this assumption, in parallel with the in-situ pump deployment, we collected two large-volume (100L) samples from the surface mixed layer at SEATS and TS1 using the onboard intake system. The samples were then passed through a column of MnO$_2$-coated acrylic fiber at a flow rate of <1 L min^{-1} to quantitatively remove Ra isotopes. ^{228}Ra activity of the samples was measured using a well-type germanium detector (ORTEC, GWL-120-15-S). Previous work found that the ^{228}Ra activities in the surface mixed layer at SEATS and TS1 were 122 ± 18 and 140 ± 13 dpm m^{-3}, respectively (Chen et al., 2010), in excellent agreement with our measurements using the MnO$_2$ cartridge method. Total ^{234}Th and dissolved ^{228}Th activities were corrected for ingrowth from their respective parent nuclides, ^{238}U and ^{228}Ra. All ^{234}Th, ^{228}Th, and ^{228}Ra data were recovery-corrected and

decay-corrected to the time of collection and reported with a propagated uncertainty that includes ±1 σ counting statistic, the uncertainty from recovery measurements, and, if applicable, the uncertainty associated with cartridge collection efficiency. Activities of ^{238}U were estimated from salinity measurements following the relationship ^{238}U (dpm L^{-1}) = 0.07081 × salinity with an assigned uncertainty of ±3% (Chen et al., 1986).

2.3. POC and primary production (PP) measurements

Size-fractionated POC was determined with a PE-2400 SERIES II CHNS/O analyzer after the removal of inorganic carbon by concentrated HCl acid fumigation for 24 h (Zhou et al., 2013). A procedural C blank of <6 μg C was determined and subtracted from final POC concentrations. The analytical precision of POC concentrations was better than 10%. The PP measurement was based on photosynthesis-irradiance (P-E) experiments using ^{14}C methods to determine the photosynthetic carbon fixation. Five or twenty μCi of NaH^{14}CO$_3$ were added to polycarbonate bottles based on the estimated phytoplankton biomass to incubate. After incubation, the actual carbon fixation rate was calculated using specific activity of ^{14}C in the medium. See Xie et al. (2015) for more details.

2.4. ^{234}Th-based POC flux

POC fluxes were estimated according to the ^{238}U—^{234}Th disequilibria method as discussed in detail by Zhou et al. (2020).

2.5. Modeling

2.5.1. POC cycling

The conceptual model of POC is displayed in Fig. 1a. The model explicitly considers two sizes of POC, small (<53 μm) and large (>53 μm), in accordance with the sampling technique that separates particles based on their size. Particles smaller than 53 μm were grouped together

and Oschlies (2008). The operator **S** assumes that sinking velocity, which is a function of remineralization rate constant r and exponent b, increases linearly with depth. The exponents b_s and b_l are optimized in the inversion. Eq. (1) describes the cycling of POC. In this model, we use square brackets to denote particle concentration or thorium activity (next section):

$$\frac{d[\text{POC}_s]}{dt} = \sigma\Gamma - r_s[\text{POC}_s] - \alpha[\text{POC}_s][\text{POC}_s] + \beta[\text{POC}_l] - \mathbf{S}_s[POC_s]$$

$$\frac{d[\text{POC}_l]}{dt} = (1-\sigma)\Gamma - r_l[\text{POC}_l] + \alpha[\text{POC}_s][\text{POC}_s] - \beta[\text{POC}_l] - \mathbf{S}_l[\text{POC}_l],$$

(1)

where α and β are particle aggregation and disaggregation rate constants, respectively; r_s and r_l are the small- and large-sized POC remineralization rate constants; subscripts l and s denote large and small particles, respectively. Γ represents model PP and is sample-specific. PP was determined at higher depth resolutions than POC and thorium. To match the POC/thorium data, we used the average of PP 10 m above and below the depth of POC/thorium were collected.

2.5.2. Thorium cycling

The conceptual model for thorium cycling is displayed in Fig. 1b. The model explicitly considers three phases of thorium: dissolved ([Th$_d$]), small particulate ([Th$_s$]), and large particulate thorium ([Th$_l$]). The decay of radioactive parents (^{238}U and ^{228}Ra, denoted using [P] in the following equations) leads to the production of dissolved thorium (^{234}Th and ^{228}Th, respectively) that is then lost via radioactive decay and adsorption onto particles. Particulate thorium is lost via desorption (reversible scavenging), particle remineralization, and sinking. Like POC, small particulate thorium can aggregate to form larger particulate thorium, and large particulate thorium can break apart to form smaller particulate thorium. Eq. (2) describes thorium cycling.

$$\frac{d[\text{Th}_d]}{dt} = \lambda([\text{P}] - [\text{Th}_d]) + (r_s + \kappa_{s2})[\text{Th}_s] + (r_l + \kappa_{l2})[\text{Th}_l] - \kappa_{s1}[\text{POC}_s][\text{Th}_d] - \kappa_{l1}[\text{POC}_l][\text{Th}_d],$$

$$\frac{d[\text{Th}_s]}{dt} = -(\lambda + r_s + \kappa_{s2})[\text{Th}_s] - \alpha[\text{Th}_s][\text{Th}_s] + \beta[\text{Th}_l] + \kappa_{s1}[\text{POC}_s][\text{Th}_d] - \mathbf{S}_s[Th_s],$$

$$\frac{d[\text{Th}_l]}{dt} = -(\lambda + r + \kappa_{l2})[\text{Th}_l] + \alpha[\text{Th}_s][\text{Th}_s] - \beta[\text{Th}_l] + \kappa_{l1}[\text{POC}_l][\text{Th}_d] - \mathbf{S}_l[\text{Th}_l],$$

(2)

to reduce the number of model parameters. POC is produced in the euphotic zone, and a parameter σ determines production allocation to small- and large-sized POC. We tried to optimize σ in the inversion, but the current datasets cannot well constrain it. In practice, the value of σ was determined according to the ratio of small-sized to total particle concentrations in the top 100 m. The σ values show small depth variations with a mean±SD of 0.87±0.08 at SEATS and 0.84±0.05 at TS1, respectively. Therefore, we fix the value of σ at their mean values. In the model, small- and large-sized particles interact via particle aggregation and disaggregation, small particles aggregate to form larger particles, and large particles disaggregate to become smaller particles. We consider that disaggregation follows first-order reaction kinetics, but that aggregation follows second-order kinetics since at least two particles have to meet and collide (Wang et al., 2019). We assume that large- and small-sized particles have different remineralization rates that are constrained in the process of inversion. Both small- and large-sized particles sink and undergo gradual remineralization. Their flux distributions are assumed to follow an exponential decay function (a.k.a., Martin curve function), and are modeled using a particle flux divergence operator (**S**) constructed based on the methodology established by Kriest

where λ is the decay constant of thorium ($\lambda_{234} = 3.33 \times 10^{-7}$ s^{-1} and $\lambda_{228} = 1.16 \times 10^{-8}$ s^{-1}). κ_{l1} and κ_{s1} are adsorption rate constants for large and small particle thorium, respectively. Similar to aggregation, we assume thorium adsorption follows second-order kinetics. κ_{l2} and κ_{s2} are desorption rate constants for large and small particulate thorium, respectively. The same set of equations can be repeated for ^{234}Th and ^{228}Th. Therefore, we have two equations for POC and six for thorium isotopes.

2.5.3. The inversion

The optimization is conducted following Wang et al. (2019). Briefly, we first assume the system is at a steady state, and the left sides of eqs. (1) and (2) vanish. We solve the steady-state equations using Newton's method due to the non-linearity caused by the second-order kinetics of adsorption and aggregation. We minimize the difference between our steady-state results and observations by optimizing a set of model parameters. However, due to the dynamic nature of eddies, the system at station TS1 was unlikely to be in a steady state at the time of sampling. We, therefore, relax the steady-state assumption by decomposing the Jacobian matrix towards the most probable parameters at the steady

Table 1
Concentration of POC, [234]Th activity, and POC flux at TS1 and SEATS.

Data name	TS1: 0–100 m	SEATS: 0–100 m	TS1: SEATS
POC inventory (1–10 μm) (mmol C m^{-2})	65.89 ± 2.56	71.00 ± 2.62	0.9
POC inventory (10–53 μm) (mmol C m^{-2})	8.75 ± 0.34	4.78 ± 0.23	1.8
POC inventory (> 53 μm) (mmol C m^{-2})	16.00 ± 0.81	10.15 ± 0.38	1.6
POC at SCM (1–10 μm) (μmol C L^{-1})	1.06 ± 0.11	0.98 ± 0.10	1.1
POC at SCM (10–53 μm) (μmol C L^{-1})	0.13 ± 0.01	0.11 ± 0.10	1.2
POC at SCM (> 53 μm) (μmol C L^{-1})	0.45 ± 0.04	0.10 ± 0.01	4.5
Integral PP (mg C m^{-2} d^{-1})	764.60 (0–55 m)	115.75 (0–82 m)	6.6
[234]Th inventory (1–10 μm) (10^2 dpm m^{-2})	12.38 ± 0.32	16.02 ± 0.32	0.8
[234]Th inventory (10 - 53 μm) (10^2 dpm m^{-2})	3.78 ± 0.04	2.79 ± 0.06	1.4
[234]Th inventory (> 53 μm) (10^2 dpm m^{-2})	5.69 ± 0.05	4.07 ± 0.06	1.4
[234]Th flux at 100 m (dpm m^{-2} d^{-1})	224.76 ± 110.95	934.48 ± 112.66	0.24
POC/[234]Th (10–53μm) (μmol C dpm^{-1})	1.31 ± 0.13	1.80 ± 0.20	0.73
POC/[234]Th (> 53μm) (μmol C dpm^{-1})	1.15 ± 0.12	2.38 ± 0.25	0.48
Large POC flux at 100 m (mmol m^{-2} d^{-1})	0.55 ± 0.28	3.90 ± 0.56	0.14

state to find their eigenvalue-eigenvector pairs (Wang et al., 2019). The eigenmode's damping rates, the real part of eigenvalues, are used to separate the solutions into weakly and strongly damping parts. Considering that a typical bloom persists for approximately a week, we use a 5-day threshold to differentiate between weakly and strongly damping modes. We nevertheless conducted tests using longer (10 days) and shorter (1 day) thresholds as well, and the results were similar (Table S1). We then add the amplitudes of the slowly damping models to the list of adjustable parameters and optimize them in the process of inversion.

3. Results and discussion

3.1. POC concentrations and fluxes

At TS1, concentrations of large-sized POC (>53 μm) were 4.5 times higher in the subsurface Chl-*a* maximum (SCM) depth when compared to SEATS. However, there was no apparent difference in small-sized (1–10 μm) POC concentrations between the two stations. The surface-to-100 m integrated POC inventories in the middle- (10–53 μm) and large-sized (>53 μm) POC at TS1 were 1.8 and 1.6 times higher, respectively, than those at SEATS. Meanwhile, the small-sized POC inventories were similar at both stations (refer to Table 1). Additionally, the concentration of pigments such as fucoxanthin (Fuco, diatom pigment) and total Chl *a* (TChl *a*) showed significant peaks at SCM in TS1 compared to SEATS (see Fig. 2 and Zhou et al., 2020 for more details). The increase in biogenic silica by 4.5-fold at the SCM layer and 3-fold for the 0-100 m integration further confirms the rise in diatom abundance at TS1. Moreover, the ^{14}C primary production at TS1 was on average 6.6 times higher than at SEATS (refer to Table 1). These observations indicate that primary production was significantly enhanced at TS1 due to nutrient intrusion mediated by the cyclonic eddy (Zhou et al., 2020). However, POC fluxes estimated using the [238]U- [234]Th method at 100 m were lower at TS1 than at SEATS (refer to Table 1 and POC flux estimation in Zhou et al. (2020)).

3.2. Parameter optimization and steady-state assumption

With a total of ten adjustable parameters in the steady-state model, plus the amplitudes of slowly damping modes in the non-steady-state model, the system, consisting of eight equations (two POC functions and six thorium functions), is an underdetermined system. To address this, we constrained the parameters using both data and prior information, following the method established by Wang et al. (2019). Two scaling factors, one for data and the other for prior, are employed to determine the relative weight of the data constraint versus prior constraint in the objective function. Fig. 3a and c display the contour of evidence for SEATS and TS1, respectively. The optimal scaling factors are those that maximize the evidence.

The optimal parameters for both the steady-state and non-steady-
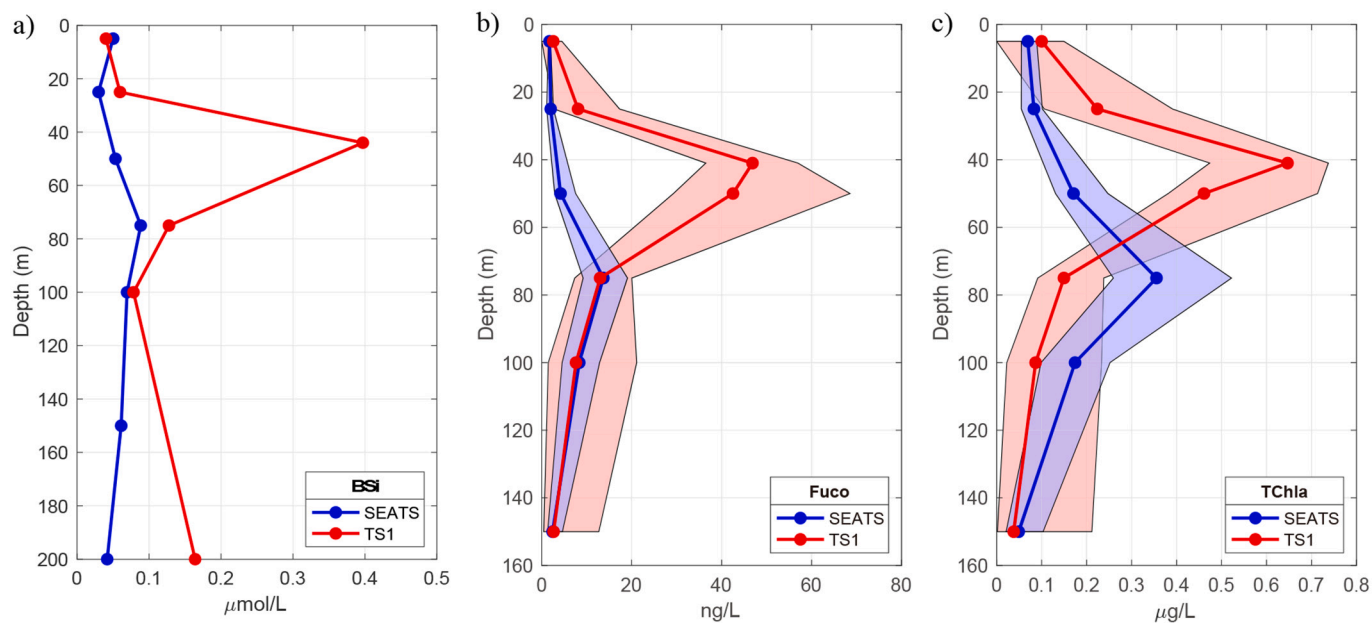
Fig. 2. Distributions of biogenic silicon (BSi, a), fucoxanthin (Fuco, b) and Chl *a* (TChla, c). The blue lines show the data from SEATS and the red lines show the data from TS1. The blue and red shades are bounded by the minimum and maximum values of the data at SEATS and TS1. (For interpretation of the references to colour in this figure legend, the reader is referred to the web version of this article.)
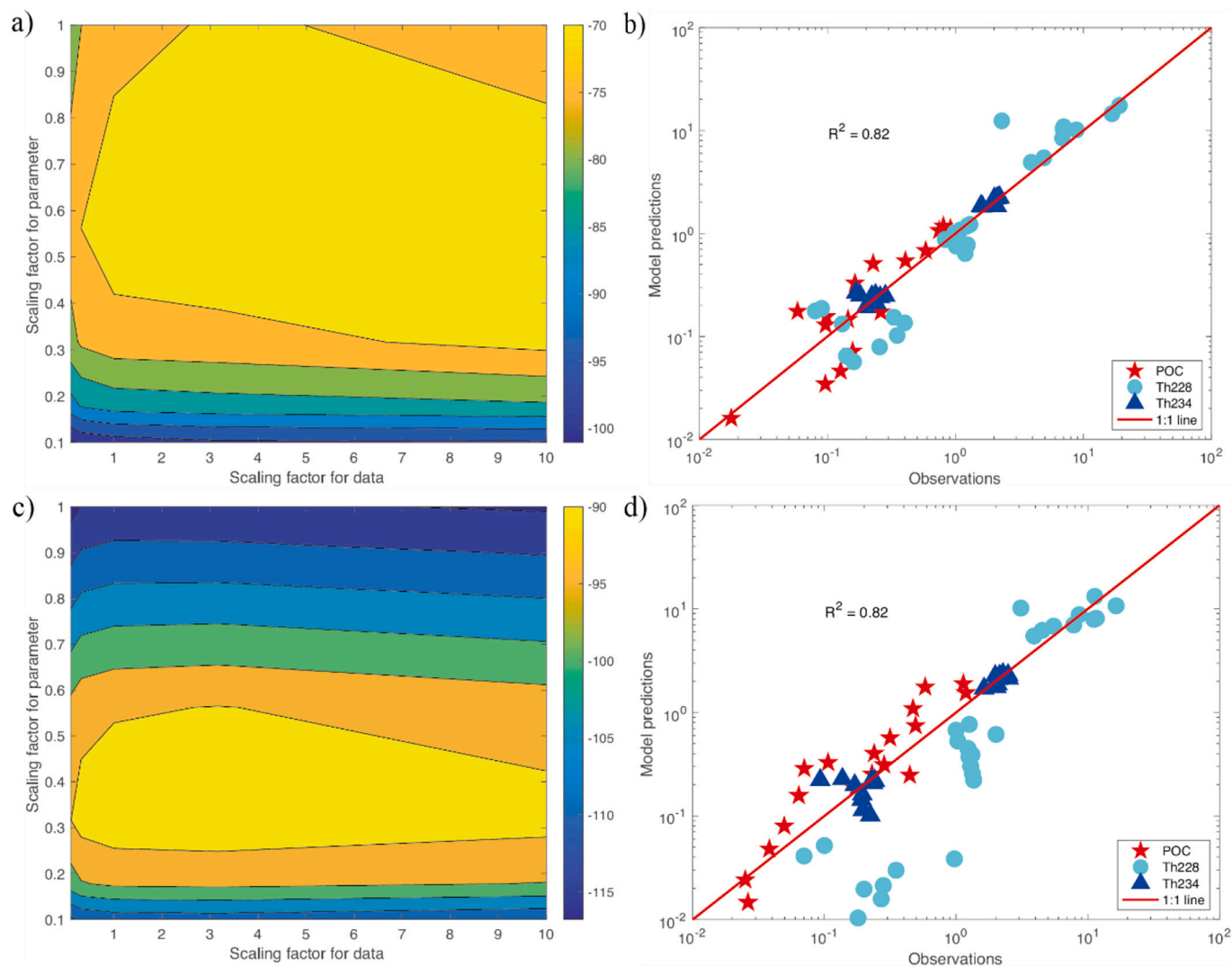
Fig. 3. Tracer-tracer plot of TS1 and SEATS. a) contour plot of the logarithm of the evidence for station SEATS. b) model versus observation comparisons of all data at station SEATS. Red stars represent POC, cyan circles stand for ^{228}Th, and blue triangles correspond to ^{234}Th. c) contour plot of the logarithm of the evidence for station TS1. d) model versus observation comparisons of all data at station TS1. The R^2 value was calculatd according to the following statistic function: $R^2 = 1 - RSS/TSS$, where RSS is sum of squared residuals and TSS is total sum of squares. Note that the x and y axis are on log scale, and R^2 is calculated according to regular values without taking logarithm. (For interpretation of the references to colour in this figure legend, the reader is referred to the web version of this article.)

Table 2

Optimal parameters. α is the aggregation rate constant; β is the disaggregation rate constant; κ_{l1} and κ_{s1} are adsorption rate constants on large and small particles; κ_{l2} and κ_{s2} are desorption rate constants from large and small particles; r_s and r_l are remineralization rate constant for small and large particles, respectively; b_s and b_l are Martin curve exponent of small and large particle. Error bars inside the square bracket correspond to $\pm 1\sigma$.

Parameters	SEATS (NSS)	TS1 (NSS)	Units
α	177.98 [123.49–256.50]	310.15 [217.99–441.26]	yr^{-1}/ (µmol L^1)
β	1175.44 [792.35–1743.74]	2115.44 [1358.82–3293.37]	yr^{-1}
κ_{l1}	2.74 [1.62–4.64]	2.04 [1.21–3.46]	yr^{-1}/ (µmol L^{-1})
κ_{l2}	4.89 [2.83–8.46]	5.09 [2.93–8.83]	yr^{-1}
κ_{s1}	2.97 [2.42–3.66]	3.15 [2.33–4.27]	yr^{-1}/ (µmol L^{-1})
κ_{s2}	2.45 [1.44–4.19]	2.80 [1.64–4.78]	yr^{-1}
r_s	1.81 [1.09–3.01]	2.37 [1.42–3.96]	yr^{-1}
r_l	68.80 [53.87–87.86]	658.92 [475.18–913.72]	yr^{-1}
b_l	0.33 [0.26–0.43]	0.82 [0.54–1.24]	unitless
b_s	0.80 [0.46–1.37]	1.04 [0.61–1.76]	unitless

state models are presented in Supplementary Table S2. It is evident that there are notable differences in the optimal parameter values between the steady-state and non-steady-state models at each station, suggesting that the system may not have been in a steady-state when the samples were collected. The subsequent discussion primarily focuses on the results obtained from the non-steady-state model.

3.3. Particle dynamics

The values of the most probable model parameters are shown in Table 2. The comparison of the key parameters with previous studies are showed in Table 3. Root mean square errors (RMSE, Table 4) are used to determine the goodness of fitting. The tracer-tracer plots are shown in Fig. 3. Overall, the model fits the observations well.

For most previous studies, aggregation and adsorption were assumed to follow first-order kinetics (e.g., Murnane et al. (1996); Murnane (1994); Nozaki et al. (1987)). In this study, we assume second-order kinetics for aggregation and adsorption because the reactions can happen only when two particles collide (Jackson, 1990; Jackson and Burd, 2015). Indeed, Wang et al. (2019) compared the difference

Table 3
Comparison of key model parameters with estimates from previous studies.

Symbol	Process	Parameters	Units	Reference
α	Aggregation	1.095 ± 0.110	m^3 $mmol^{-1}$ yr^{-1}	(Amaral et al., 2022)
		6.205 ± 7.3	m^3 $mmol^{-1}$ yr^{-1}	(Amaral et al., 2022)
		177.98 [123.49–256.50]	m^3 $mmol^{-1}$ yr^{-1}	SEATS in this study
		310.15 [217.99–441.26]	m^3 $mmol^{-1}$ yr^{-1}	TS1 in this study
β	Disaggregation	90 ± 15–630 ± 190	yr^{-1}	(Lavelle et al., 1991)
		148 ± 370–788 ± 1400	yr^{-1}	(Nozaki et al., 1987)
		~ 62	yr^{-1}	(Nozaki et al., 1987)
		~ 65	yr^{-1}	(Clegg et al., 1991)
		156.95 ± 18.25	yr^{-1}	(Murnane et al., 1996)
		15– 6500	yr^{-1}	(Clegg et al., 1991)
		0.30 ± 0.08	yr^{-1}	(Wang et al., 2016a)
		1175.44 [792.35–1743.74]	yr^{-1}	SEATS in this study
		2115.44 [1358.82–3293.37]	yr^{-1}	TS1 in this study
r	Remineralization	36.5 ± 18.3 (for small)	yr^{-1}	(Clegg et al., 1991)
		54.75 ± 27.38 (for large)	yr^{-1}	(Santoro et al., 2020)
		1.81 [1.09–3.01]	yr^{-1}	Small Remi. in SEATS
		68.80 [53.87–87.86]	yr^{-1}	Large Remi. in SEATS
		2.37 [1.42–3.96]	yr^{-1}	Small Remi. in TS1
		658.92 [475.18–913.72]	yr^{-1}	Large Remi. in TS1

Table 4
Root mean square errors (RMSE) between observations and model predictions.

Station	^{228}Th (dpm m^{-3})	^{234}Th (dpm L^{-1})	POC (μmol C L^{-1})
TS1	0.35	0.030	0.20
SEATS	0.59	0.011	0.074

between first- and second-order kinetics and found that the second-order kinetics fit their observations better.

Our estimates of aggregation rate constants at SEATS and TS1 are 177.98 [123.49–256.50] (mmol m^{-3})$^{-1}$ yr^{-1} (0.49 [0.34–0.70] (mmol m^{-3})$^{-1}$ d^{-1}) and 310.15 [217.99–441.26] (mmol m^{-3})$^{-1}$ yr^{-1} (0.86 [0.60–1.21] (mmol m^{-3})$^{-1}$ d^{-1}), respectively. A recent study by Amaral et al. (2022) obtained much lower 2nd-order kinetic aggregation rate constants of 1.10 ± 0.11 (mmol m^{-3})$^{-1}$ yr^{-1} (0.003 ± 0.0003 (mmol m^{-3})$^{-1}$ d^{-1}) in the upper 500 m at Station P in the North Atlantic. However, their estimates were primarily determined by the priors obtained by dividing a first-order aggregation rate constant from one study (Murnane et al., 1996) by POC concentration from another study (Bishop et al., 1999). Using chloropigment and POC as tracers, Wang et al. (2019) estimated a 2nd-order aggregation rate constant of 2.78 (mmol m^{-3})$^{-1}$ yr^{-1} (0.008 (mmol m^{-3})$^{-1}$ d^{-1}) for samples collected below 100 m in the Mediterranean Sea. The aggregation rate constant in Wang et al. (2019) may be low because the remineralization of organic matter reduces the stickiness of particles. To our knowledge, there are

no other studies estimating 2nd-order kinetic aggregation rate constants except for the above two references. Here we advocate for more studies on this important parameter.

Our estimates of disaggregation rate constants at SEATS and TS1 are 1175.44 [792.35–1743.74] yr^{-1} (3.21 [2.17–4.78] d^{-1}) and 2115.44 [1358.82–3293.37] yr^{-1} (5.79 [3.72–9.02]d^{-1}), respectively. Published disaggregation rate constants have a very large range (0.30–6500 yr^{-1}, 0.001–17.81 d^{-1}) (Wang et al., 2016a). For example, Nozaki et al. (1987) reported a range of disaggregation rate constants of 148 ± 370–788 ± 1400 yr^{-1} (0.41 ± 1.01–2.16 ± 3.84 d^{-1}) at the Western Pacific. Lavelle et al. (1991) found disaggregation rate constants between 90 ± 15 to 630 ± 190 yr^{-1} (0.25 ± 0.04–1.73 ± 0.52 d^{-1}) in Puget Sound. Nozaki et al. (1987) obtained 62 yr^{-1} (0.17 d^{-1}) in the Western Pacific and Clegg et al. (1991) reported 65 yr^{-1} (0.18 d^{-1}) for a North Pacific station. Two recent studies by Wang et al. (2019) and Amaral et al. (2022) conducted at the DYFAMED station in the Mediterranean Sea and the Station P in the western Pacific Ocean, respectively, reported disaggregation rate constants of 0.13–0.41 d^{-1} and 0.43 ±0.05 d^{-1}. Our estimates align closely with those reported by Nozaki et al. (1987) and are higher than the values reported in the other studies. The disparities between current study and previous investigations may be attributed, in part, to geographical variations. This could also be due to the fact that our model covers the whole euphotic zone, in which fresh phytoplankton aggregates are more fragile and susceptible to disaggregation due to selective feeding by zooplankton (Briggs et al., 2020).

Similarly, previously reported remineralization rate constants exhibit a fairly large range from 1.5–73 yr^{-1} (0.004–0.20 d^{-1}) (Wang et al., 2019). In an inversion using thorium and POC as tracers, Wang et al. (2017) estimated a remineralization rate constant of 1.5 yr^{-1} (0.004 d^{-1}) for slow-sinking particles collected using Indented Rotating Spheric (IRS) sinking-velocity sediment traps deployed below 300 m at the Mediterranean Sea. In another inversion using chloropigment as tracers, Wang et al. (2019) reported a remineralization rate constant of 2.44 yr^{-1} (0.0067 d^{-1}) for small particles (1–70μm). Clegg et al. (1991) reported a remineralization rate constant of 36.5 ± 18.2 yr^{-1} (0.1 ± 0.05 d^{-1}) for the small particles in the equatorial Pacific. Santoro et al. (2020) estimated that a high particle remineralization rate constant of 54.75 ± 27.38 yr^{-1} (0.15 ± 0.075 d^{-1}) in the North Pacific, which is higher than reported rate constants for small particles. Murnane et al. (1996) estimated a remineralization rate constant of 77 ± 10 yr^{-1} based on data collected in the JGOFS North Atlantic Bloom Experiment between 100 and 400 m. Our estimates of small particle remineralization rate constants in this study (1.81 [1.09–3.01] yr^{-1} (0.005 [0.003–0.008] d^{-1}) at SEATS, 2.37 [1.42–3.96] yr^{-1} (0.0065 [0.0039–0.011] d^{-1}) at TS1) are at the lower end of the previously reported ranges. For large particles, the remineralization rate constant at SEATS (68.80 [53.87–87.86] yr^{-1}, 0.19 [0.15–0.24] d^{-1}) is near the higher end of previous estimates, the rate constant at TS1 (658.92 [475.18–913.72] yr^{-1}, 1.81 [1.30–2.50] d^{-1}) is 9.6 times that of SEATS, and also higher than any previously reported values. This discrepancy could potentially be attributed to highly efficient microbial loop at TS1 or to processes that are not accounted for in our model.

3.4. The effect of the decaying cyclonic eddies on carbon export

Compared to SEATS, both aggregation and disaggregation rates are higher at TS1 (Fig. 4 and Table 5), indicating that particle "exchanges" are stronger at TS1. Comparisons of aggregation and disaggregation rates show that disaggregation rates at TS1 are higher than aggregation rates (except at 25 m; see Table 5), which suggests that there were more particles breaking apart to form smaller particles than the opposite. Particle fragmentation or disaggregation leads to particles with slower settling velocity and longer residence time in the upper ocean (Wang and Fennel, 2022). We found that both disaggregation rate for large particles and remineralization rates for both large and small particles at TS1 were higher than at SEATS (Fig. 4 and Table 5), which indicates that
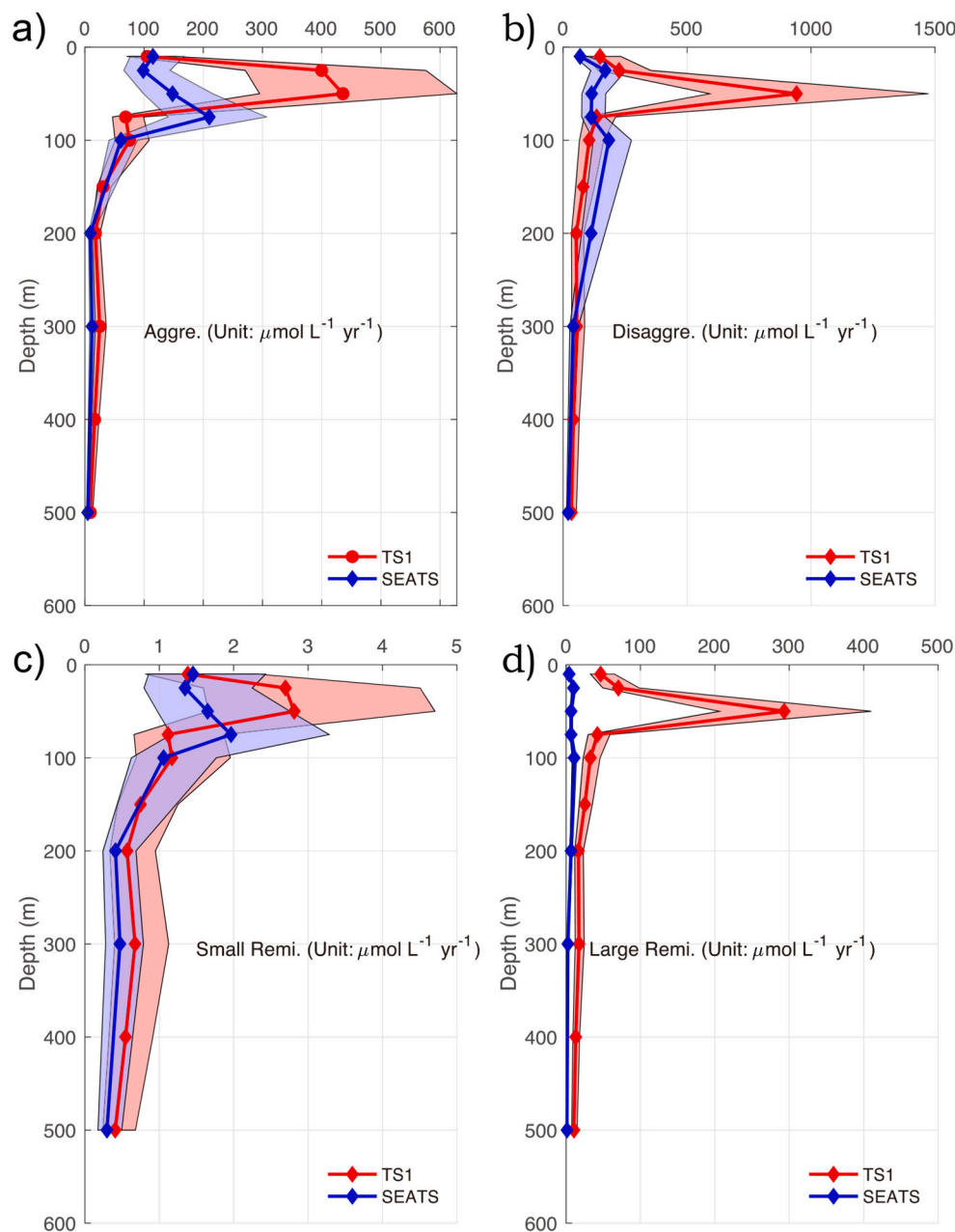
Fig. 4. Profile of particle cycling rates. a) aggregation rates. b) disaggregation rates. c) remineralization rate for small particles. d) remineralization rate for large particles. In each figure, the red line shows the rate distribution at TS1 station and the blue line shows the rate distribution at SEATS station. The red and blue shaded regions represent $\pm 1 \sigma$. Note that the exchange rates are the products of rate constants and particle concentrations. Although the rate constants (e. g., aggregation rate constants and remineralization rate constant) are different, the particle concentrations are the same. Therefore, the final results display a similar pattern but on different scales. (For interpretation of the references to colour in this figure legend, the reader is referred to the web version of this article.)

fragmentation and remineralization was enhanced in the cyclonic eddy (TS1). The higher remineralization rate of large particles is even more evident at TS1. After particle fragmentation and remineralization, the suspended smaller particles or inorganic nutrients should be transported out of the studied domain by lateral transport or deep mixing. The comparison between the steady-state model and non-steady-state model indicates that both study stations underwent non-steady-state transport conditions during the sampling period. To summarize, our model results suggest that stronger large-particle disaggregation and remineralization together reduce POC export despite higher productivity in the cyclonic eddy.

It is generally believed that cyclonic eddies upwell high concentrations of nutrients from below the thermocline to the euphotic zone and therefore support a high primary production (McGillicuddy Jr, 2016), which can further stimulate high carbon export. In support of this, Vaillancourt et al. (2003) found that large photosynthetic eukaryotes are more abundant inside an eddy compared to non-eddy-impacted regions. In the South China Sea, Guo et al. (2015) demonstrated cyclonic eddies

enhanced the nutrient concentrations, and altered the abundance of phytoplankton and zooplankton. Particularly because of the abundant silicate, diatoms were the most enhanced phytoplankton in the eddy center (Wang et al., 2016b). A similar conclusion was drawn by Bibby and Moore (2011), who suggested that the phytoplankton community structure maintained by mesoscale eddies is determined by the relative abundances of silicates and nitrates. Similarly, we find that primary production was higher in the center of the cyclonic eddy (TS1) than in the nearby oligotrophic SEATS station. Surprisingly, we also find that POC flux was not enhanced at TS1 compared to SEATS. Our model results suggest that this is mainly due to strong disaggregation and remineralization at TS1, possibly related to higher bacterial respiration during the decay stage of the cyclonic eddy (Zhou et al., 2020). In support of the above hypothesis, the diatom model of Grossart and Ploug (2001) demonstrates that the aggregate-attached food webs significantly increase POC transformation and remineralization, which can reduce the sinking export flux.

Table 5
Key rates at SEATS and TS1. Numbers in square brackets represent error estimates correspond to ±1σ.

Depth (m)	Aggregation (μmol L^{-1} yr^{-1})		Disaggregation (μmol L^{-1} yr^{-1})		Large Remi. (μmol L^{-1} yr^{-1})		Small Remi. (μmol L^{-1} yr^{-1})	
	SEATS	TS1	SEATS	TS1	SEATS	TS1	SEATS	TS1
10	114.88 [76.46–167.87]	105.22 [71.26–151.63]	68.51 [45.16–102.33]	148.79 [93.53–232.96]	4.01 [3.05–5.19]	46.34 [32.62–64.86]	1.45[0.86 –2.43]	1.38 [0.82–2.31]
25	98.56 [65.76–143.91]	399.82 [271.02–576.01]	169.88 [111.97–253.75]	225.68 [141.87–353.35]	9.94 [7.57–12.87]	70.30 [49.47–98.37]	1.35 [0.79–2.25]	2.70 [1.60–4.51]
50	148.05 [98.86–216.11]	435.85 [295.01–628.23]	115.03 [75.82–171.82]	941.29 [591.71–1473.81]	6.73 [5.12–8.72]	293.20 [206.34–410.30]	1.65 [0.97–2.76]	2.81 [1.66–4.71]
75	210.05 [140.34–306.56]	68.81 [46.60–99.17]	113.49 [74.80–169.52]	135.24 [85.02–211.76]	6.64 [5.06–8.60]	42.13 [29.65–58.95]	1.96 [1.16–3.28]	1.12 [0.66–1.87]
100	60.88 [40.74–88.81]	75.23 [50.95–108.42]	184.53 [121.62–275.63]	104.87 [65.93–164.20]	10.80 [8.22–13.98]	32.67 [22.99–45.71]	1.06 [0.63–1.77]	1.17 [0.69–1.95]
150	–	30.79 [20.86–44.37]	–	80.84 [50.82–126.57]	–	25.18 [17.72–35.24]	–	0.75 [0.44–1.25]
200	9.19[6.16–13.39]	17.68 [12.03–25.43]	112.90 [74.41–168.64]	53.05[33.35–83.06]	6.61 [5.03–8.55]	16.52 [11.63–23.12]	0.41 [0.24–0.69]	0.57 [0.34–0.95]
300	12.05[8.07–17.57]	25.00 [16.99–35.98]	41.28 [27.20–61.66]	55.65[34.98–87.13]	2.42 [1.84–3.13]	17.33 [12.20–24.26]	0.47 [0.28–0.79]	0.67 [0.40–1.13]
400	–	16.39 [11.14–23.59]	–	41.51[26.09–64.99]	–	12.93[9.10–18.09]	–	0.55 [0.32–0.91]
500	4.77[3.19–6.96]	9.10[6.18–13.10]	20.78 [13.70–31.04]	33.92[21.33–53.12	1.22 [0.93–1.57]]	10.57[7.44–14.79]	0.30 [0.18–0.49]	0.41 [0.24–0.68]
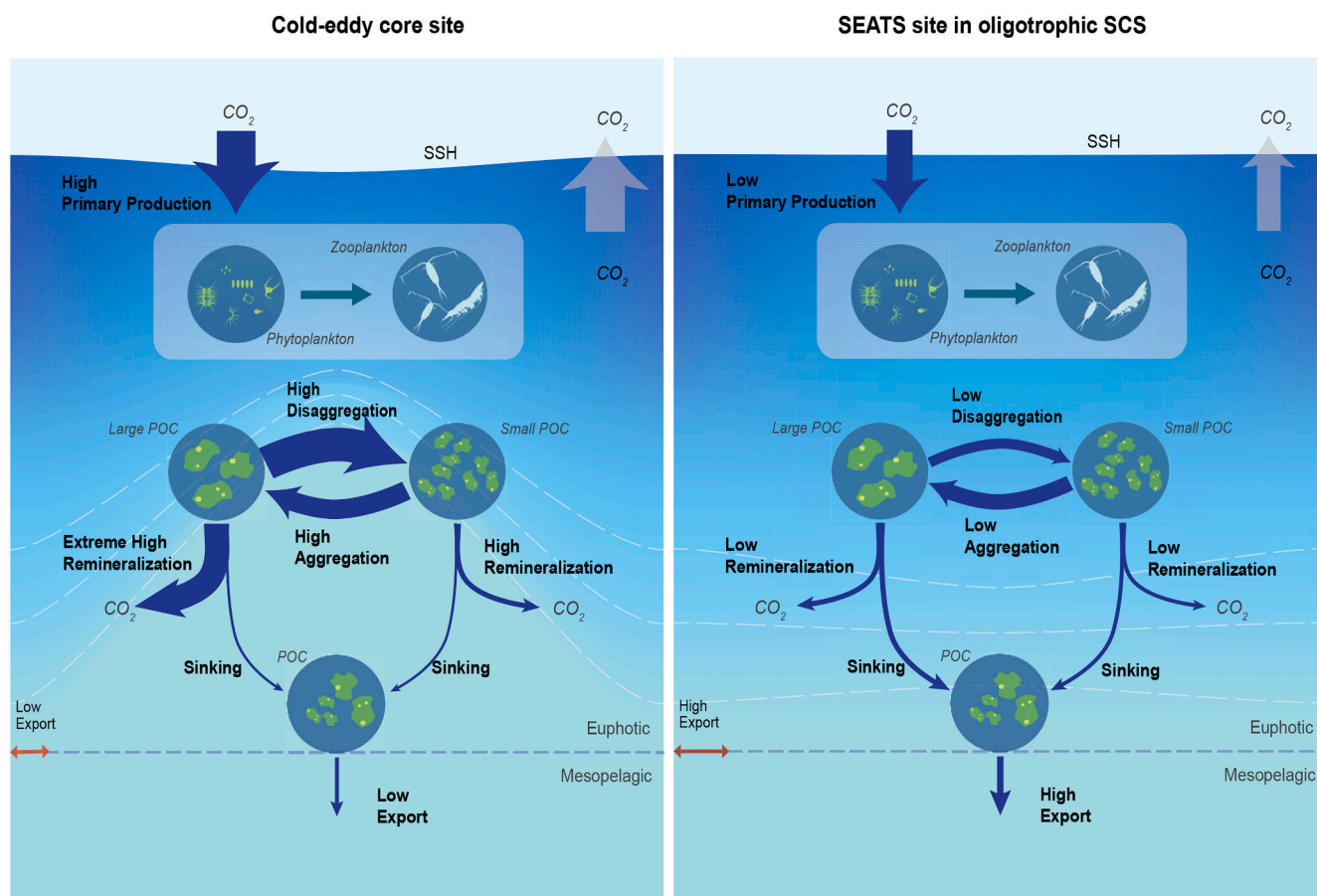
Fig. 5. Schematic diagram of the production, remineralization, and export in the eddy-impacted region (left) and non-eddy-impacted region (right). The thickness of the arrow represents the rate/flux. The diagram shows that in the eddy-impacted region, the strong aggregation, disaggregation, and remineralization rate together generate a faster cycling circle compared to in the non-eddy-impacted region.

4. Conclusion

In this study, we conducted a comparison of particle dynamics between two stations: one located in the center of a cyclonic eddy (TS1) during the decay stage, and the other in a nearby oligotrophic ocean in the South China Sea (SEATS). Our findings show that the higher rates of disaggregation and remineralization at TS1 led to a reduction in carbon export, resulting in lower export fluxes compared to SEATS, even though

production at TS1 was higher. Our results suggest that the decaying cyclonic eddy accelerated the production-fragmentation-remineralization cycle when compared to the non-eddy impacted region (see Fig. 5), which allowed particles to be rapidly disaggregated and remineralization, reducing the vertical export of particles. This discovery may have implications for the counterintuitive relationship between high biomass and low export efficiency that has been observed in the Southern Ocean and other high production upwelling regions (Cavan et al., 2015; Henson et al., 2012; Lam and Bishop, 2007; Maiti et al., 2013). Prior explanations for this relationship include strong particle remineralization in the surface ocean, zooplankton-mediated export, a time lag between production and export, and export conducted by dissolved organic carbon (Laws and Maiti, 2019; Le Moigne et al., 2016). Our current study along with the finding of Briggs et al. (2020) suggest that particle fragmentation determines the depth of organic carbon remineralization. We therefore suggest that particle dynamics could also be a possible mechanism to explain the phenomenon of high primary production and low POC export efficiency.

Code availability

All the codes will be available before publication upon request.

Data availability

Raw data and model output can be accessed through the following link: https://doi.org/10.6084/m9.figshare.21819990.v1.

Acknowledgment

Appendix A. Supplementary data

Supplementary data to this article can be found online at https://doi.org/10.1016/j.marchem.2023.104279.

References

Amaral, V.J., Lam, P.J., Marchal, O., Roca-Martí, M., Fox, J., Nelson, N.B., 2022. Particle cycling rates at station P as estimated from the inversion of POC concentration data. Elementa: Sci. Anthropocen. 10 (1) https://doi.org/10.1525/elementa.2021.00018.

Benitez-Nelson, C.R., Bidigare, R.R., Dickey, T.D., Landry, M.R., Leonard, C.L., Brown, S. L., Nencioli, F., Rii, Y.M., Maiti, K., Becker, J.W., 2007. Mesoscale eddies drive increased silica export in the subtropical Pacific Ocean. Science 316 (5827), 1017–1021.

Bibby, T., Moore, C., 2011. Silicate: nitrate ratios of upwelled waters control the phytoplankton community sustained by mesoscale eddies in sub-tropical North Atlantic and Pacific. Biogeosciences 8 (3), 657–666.

Bishop, K.B., Calvert, J.E.S., Soon, M.Y.S., 1999. Spatial and temporal variability of POC in the northeast subarctic Pacific. Deep-Sea Res. II Top. Stud. Oceanogr. 46 (11−12), 2699–2733. https://doi.org/10.1016/s0967-0645(99)00081-8.

Boyd, P., Trull, T., 2007. Understanding the export of biogenic particles in oceanic waters: is there consensus? Prog. Oceanogr. 72 (4), 276–312.

Briggs, N., Dall'Olmo, G., Claustre, H., 2020. Major role of particle fragmentation in regulating biological sequestration of CO$_2$ by the oceans. Science 367 (6479), 791–793.

Cai, P., Dai, M., Chen, W., Tang, T., Zhou, K., 2006. On the importance of the decay of ^{234}Th in determining size-fractionated C/^{234}Th ratio on marine particles. Geophys. Res. Lett. 33 (23).

Cavan, E.L., Le Moigne, F.A.C., Poulton, A.J., Tarling, G.A., Ward, P., Daniels, C.J., Fragoso, G.M., Sanders, R.J., 2015. Attenuation of particulate organic carbon flux in the Scotia Sea, Southern Ocean, is controlled by zooplankton fecal pellets. Geophys. Res. Lett. 42 (3), 821–830. https://doi.org/10.1002/2014gl062744.

Charette, M.A., Dulaiova, H., Gonneea, M.E., Henderson, P.B., Moore, W.S., Scholten, J. C., Pham, M.K., 2012. GEOTRACES radium isotopes interlaboratory comparison experiment. Limnol. Oceanogr. Methods 10 (6), 451–463. https://doi.org/10.4319/lom.2012.10.451.

Chen, J., Edwards, R.L., Wasserburg, G.J., 1986. ^{238}U, ^{234}U and ^{232}Th in seawater. Earth Planet. Sci. Lett. 80 (3–4), 241–251.

Chen, W., Liu, Q., Huh, C.A., Dai, M., Miao, Y.C., 2010. Signature of the Mekong River plume in the western South China Sea revealed by radium isotopes. J. Geophys. Res. Oceans 115 (C12).

Ciais, P., Sabine, C., Bala, G., Bopp, L., Brovkin, V., Canadell, J., Chhabra, A., DeFries, R., Galloway, J., Heimann, M., 2014. Carbon and other biogeochemical cycles. In: Climate Change 2013: The Physical Science Basis. Contribution of Working Group I to the Fifth Assessment Report of the Intergovernmental Panel on Climate Change. Cambridge University Press, pp. 465–570.

Clegg, S.L., Bacon, M., Whitfield, M., 1991. Application of a generalized scavenging model to thorium isotope and particle data at equatorial and high-latitude sites in the Pacific Ocean. J. Geophys. Res. Oceans 96 (C11), 20655–20670.

Falkowski, P.G., Ziemann, D., Kolber, Z., Bienfang, P.K., 1991. Role of eddy pumping in enhancing primary production in the ocean. Nature 352 (6330), 55–58.

Grossart, H.-P., Ploug, H., 2001. Microbial degradation of organic carbon and nitrogen on diatom aggregates. Limnol. Oceanogr. 46 (2), 267–277. https://doi.org/10.4319/lo.2001.46.2.0267.

Guidi, L., Legendre, L., Reygondeau, G., Uitz, J., Stemmann, L., Henson, S.A., 2015. A new look at ocean carbon remineralization for estimating Deepwater sequestration. Glob. Biogeochem. Cycles 29 (7), 1044–1059.

Guo, M., Chai, F., Xiu, P., Li, S., Rao, S., 2015. Impacts of mesoscale eddies in the South China Sea on biogeochemical cycles. Ocean Dyn. 65 (9), 1335–1352.

Henson, S.A., Sanders, R., Madsen, E., Morris, P.J., Le Moigne, F., Quartly, G.D., 2011. A reduced estimate of the strength of the ocean's biological carbon pump. Geophys. Res. Lett. 38 (4).

Henson, S.A., Sanders, R., Madsen, E., 2012. Global patterns in efficiency of particulate organic carbon export and transfer to the deep ocean. Glob. Biogeochem. Cycles 26 (1).

Jackson, G.A., 1990. A model of the formation of marine algal flocs by physical coagulation processes. Deep Sea Rese. Part A. Oceanograph. Res. Pap. 37 (8), 1197–1211.

Jackson, G.A., Burd, A.B., 2015. Simulating aggregate dynamics in ocean biogeochemical models. Prog. Oceanogr. 133, 55–65.

Kriest, I., Oschlies, A., 2008. On the treatment of particulate organic matter sinking in large-scale models of marine biogeochemical cycles. Biogeosciences 5 (1), 55–72.

Lam, P.J., Bishop, J.K.B., 2007. High biomass, low export regimes in the Southern Ocean. Deep-Sea Res. II Top. Stud. Oceanogr. 54 (5–7), 601–638. https://doi.org/10.1016/j.dsr2.2007.01.013.

Lavelle, J., Cokelet, E., Cannon, G., 1991. A model study of density intrusions into and circulation within a deep, silled estuary: Puget Sound. J. Geophys. Res. Oceans 96 (C9), 16779–16800.

Laws, E.A., Maiti, K., 2019. The relationship between primary production and export production in the ocean: effects of time lags and temporal variability. Deep-Sea Res. I Oceanogr. Res. Pap. 148, 100–107. https://doi.org/10.1016/j.dsr.2019.05.006.

Le Moigne, F.A.C., Henson, S.A., Cavan, E., Georges, C., Pabortsava, K., Achterberg, E.P., Ceballos-Romero, E., Zubkov, M., Sanders, R.J., 2016. What causes the inverse relationship between primary production and export efficiency in the Southern Ocean? Geophys. Res. Lett. 43 (9), 4457–4466. https://doi.org/10.1002/2016gl068480.

Le Quéré, C., Andrew, R.M., Friedlingstein, P., Sitch, S., Hauck, J., Pongratz, J., Pickers, P.A., Korsbakken, J.I., Peters, G.P., Canadell, J.G., 2018. Global carbon budget 2018. Earth Syst. Sci. Data 10 (4), 2141–2194.

Luo, S., Ku, T.-L., Kusakabe, M., Bishop, J.K., Yang, Y.-L., 1995. Tracing particle cycling in the upper ocean with ^{230}Th and ^{228}Th: an investigation in the equatorial Pacific along 140 W. Deep-Sea Res. II Top. Stud. Oceanogr. 42 (2–3), 805–829.

Maiti, K., Charette, M.A., Buesseler, K.O., Kahru, M., 2013. An inverse relationship between production and export efficiency in the Southern Ocean. Geophys. Res. Lett. 40 (8), 1557–1561. https://doi.org/10.1002/grl.50219.

Martin, J.H., Knauer, G.A., Karl, D.M., Broenkow, W.W., 1987. VERTEX: carbon cycling in the Northeast Pacific. Deep Sea Res. Part A Oceanograph. Res. Papers 34 (2), 267–285.

McGillicuddy Jr., D.J., 2016. Mechanisms of physical-biological-biogeochemical interaction at the oceanic mesoscale. Annu. Rev. Mar. Sci. 8, 125–159.

McGillicuddy, D., Robinson, A., Siegel, D., Jannasch, H., Johnson, R., Dickey, T., McNeil, J., Michaels, A., Knap, A., 1998. Influence of mesoscale eddies on new production in the Sargasso Sea. Nature 394 (6690), 263–266.

Murnane, R.J., 1994. Determination of thorium and particulate matter cycling parameters at station P: A reanalysis and comparison of least squares techniques. J. Geophys. Res. Oceans 99 (C2), 3393–3405.

Murnane, R., Cochranj, J., Buesseler, K., Bacon, M., 1996. Least-squares estimates of thorium, particle, and nutrient cycling rate constants from the JGOFS North Atlantic bloom experiment. Deep-Sea Res. I Oceanogr. Res. Pap. 43 (2), 239–258.

Nozaki, Y., Yang, H.S., Yamada, M., 1987. Scavenging of thorium in the ocean. J. Geophys. Res. Oceans 92 (C1), 772–778.

Santoro, A., Albers, J., Durkin, C.A., Bressac, M., Estapa, M.L., Buesseler, K., Omand, M., Passow, U., Boyd, P.W., 2020. Microbial community composition on sinking particles as a function of depth and particle type in the North Pacific. Ocean Sci. Meet. 2020.

Siegel, D., Buesseler, K., Doney, S.C., Sailley, S., Behrenfeld, M.J., Boyd, P., 2014. Global assessment of ocean carbon export by combining satellite observations and food-web models. Glob. Biogeochem. Cycles 28 (3), 181–196.

Siegel, D.A., DeVries, T., Cetinić, I., Bisson, K.M., 2023. Quantifying the Ocean's biological pump and its carbon cycle impacts on global scales. Annu. Rev. Mar. Sci. 15 (1), null. https://doi.org/10.1146/annurev-marine-040722-115226.

Vaillancourt, R.D., Marra, J., Seki, M.P., Parsons, M.L., Bidigare, R.R., 2003. Impact of a cyclonic eddy on phytoplankton community structure and photosynthetic competency in the subtropical North Pacific Ocean. Deep-Sea Res. I Oceanogr. Res. Pap. 50 (7), 829–847.

Wang, B., Fennel, K., 2022. Biogeochemical-Argo data suggest significant contributions of small particles to the vertical carbon flux in the subpolar North Atlantic. Limnol. Oceanogr. 67 (11), 2405–2417.

Wang, W.-L., Armstrong, R.A., Cochran, J.K., Heilbrun, C., 2016a. 230 Th and 234 Th as coupled tracers of particle cycling in the ocean: a maximum likelihood approach. Deep Sea Res. PT I 111, 61–70. https://doi.org/10.1016/j.dsr.2016.02.003.

Wang, L., Huang, B., Chiang, K.-P., Liu, X., Chen, B., Xie, Y., Xu, Y., Hu, J., Dai, M., 2016b. Physical-biological coupling in the western South China Sea: the response of phytoplankton community to a mesoscale cyclonic eddy. PLoS One 11 (4), e0153735.

Wang, W.-L., Lee, C., Cochran, J.K., Primeau, F.W., Armstrong, R.A., 2017. A novel statistical analysis of chloropigment fluxes to constrain particle exchange and organic matter remineralization rate constants in the Mediterranean Sea. Mar. Chem. 192, 49–58. https://doi.org/10.1016/j.marchem.2017.03.011.

Wang, W.-L., Lee, C., Primeau, F.W., 2019. A Bayesian statistical approach to inferring particle dynamics from in-situ pump POC and chloropigment data from the Mediterranean Sea. Mar. Chem. 214, 103654 https://doi.org/10.1016/j.marchem.2019.04.006.

Xie, Y., Huang, B., Lin, L., Laws, E.A., Wang, L., Shang, S., Zhang, T., Dai, M., 2015. Photosynthetic parameters in the northern South China Sea in relation to phytoplankton community structure. J. Geophys. Res. Oceans 120 (6), 4187–4204. https://doi.org/10.1002/2014JC010415.

Zhou, K., Dai, M., Kao, S.-J., Wang, L., Xiu, P., Chai, F., Tian, J., Liu, Y., 2013. Apparent enhancement of [234]Th-based particle export associated with anticyclonic eddies. Earth Planet. Sci. Lett. 381, 198–209.

Zhou, K., Dai, M., Xiu, P., Wang, L., Hu, J., Benitez-Nelson, C.R., 2020. Transient enhancement and decoupling of carbon and opal export in cyclonic eddies. J. Geophys. Res. Oceans 125 (9) e2020JC016372.